J. Earth Syst. Sci. (2020)129 67
https://doi.org/10.1007/s12040-019-1310-7

Analysis of seismic site characterization of the Isparta basin (southwestern Turkey) using passive surface-wave method (ReMi^{TM}) and borehole data

Ali Silahtar[1], Mehmet Zakir Kanbur[2,*] and Günay Beyhan[1]

[1]*Department of Geophysical Engineering, Sakarya University, Sakarya, Turkey.*
[2]*Department of Geophysical Engineering, Suleyman Demirel University, Isparta, Turkey.*
**Corresponding author. e-mail: zakirkanbur@sdu.edu.tr*

MS received 21 June 2018; revised 4 July 2019; accepted 10 October 2019

This study presents a site classification of the Isparta basin situated at the upper part of the Isparta Angle, which is one of the most important tectonic components in Turkey. The local conditions of the basin sediments may significantly increase ground motions from earthquakes and cause more structural damage. V_{s30} is one of the base parameters used for the determining site classification. In this study, refraction microtremor (ReMi^{TM}) method was used to determine the shear-wave velocities structure and hence classifying the site characterization of Isparta basin. The data were collected at 172 locations and converted to shear-wave velocity–depth models and shear velocity (V_s) maps were created. The V_s structures were compared and evaluated with the current borehole records compiled from the area. The site classification map of the Isparta basin was prepared by using the V_{s30} map and considering the National Earthquake Hazards Reduction Program (NEHRP) criteria. According to this map, the soft alluvial deposits of the central basin are mostly classified as D, and a few are classified as C. The soil class at the southern part of the basin (old urbanization area of the city) increases to C class due to which the tuff–tuffite content increases. The rock units such as Mesozoic carbonates and Cenozoic flysch located around the basin are classified as A. The soil class B, appears between the class A rocks and the alluvial basin, has relatively thin alluvial slope deposit overlying the rock. The classification obtained from this study may contribute to the studies on future urban planning and seismic risk assessment.

Keywords. ReMi^{TM} (Refraction microtremor); seismic risk assessment; site characterization; V_{s30}; Isparta basin.

1. Introduction

The rapid growth of the population as well as migration to cities from rural in Turkey has led to the construction of buildings and infrastructure in urban areas. A similar problem in Isparta is concerned. The tendency of developing constructions on sedimentary basins, and rapid and unplanned urbanization have reduced the safety of the structures built at such areas that have earthquake risk. Therefore, the studies of site effect are very important, and it is essential to be considered for such areas. Destructive earthquakes, such as the 1999 Kocaeli event (M_w 7.4), the 1999 Düzce event (M_w 7.2), and the 2011 Van event (M_w 7.2), which recently occurred in Turkey, have clearly showed that the local soil conditions may have a primary effect for destruction.

Soil classification of urban area is one of the required works to minimize the possible destruction

Published online: 07 February 2020

caused by earthquake effects (Stephenson *et al.* 2005; Poormirzaee and Moghadam 2014; Pancha *et al.* 2017a). The engineering characteristics of the distribution of soil accumulation are the required information for civil engineering and urban planning. Several studies showed that the shear-wave velocity is a key parameter for evaluating the ground motion (Borcherdt 1970; Stephenson *et al.* 2005; Odum *et al.* 2013; Silahtar *et al.* 2016).

The site characterization studies are based on the effects of the soil types related with ground motion response. At that point, the dominant frequency is a very important factor that controls the amplification of ground motions. Two factors play an important role for dominant frequency to be formed. These are the shear-wave velocity and the soil thickness (Rodriguez-Marek *et al.* 2001). Borcherdt (1994) showed that the average shear-wave velocity of the uppermost 30 m of the soil section (V_{s30}) is the most effective value for the site characterization. In the known building codes such as Uniform Building Code (UBC97), Eurocode 8 (Code 2005) and NEHRP (Building Seismic Safety Council (BSSC) 2003), V_{s30} criteria are used for site classification. Anderson *et al.* (1996) and Abrahamson and Silva (2008) also used V_{s30} as a site classification parameter for creating their attenuation model and determining the depth of engineering bedrock.

S-wave (V_s) structure of the shallow depth of the soil may be quickly obtained by the refraction microtremor (ReMi^{TM}) method (Louie 2001). The method is based on ambient noise measurements that are performed with seismic arrays to obtain information on surface wave velocity dispersion. Forward or inversion solution of the dispersion curves provides a one-dimensional shear-wave velocity (V_s) models down to a depth related to the length of the array.

In this study, it was aimed to apply this method to Isparta basin that covers the city of Isparta, urban regeneration, industrial buildings, and the Isparta airport. The routes having higher cultural noise were typically preferred for the data recording. As a result, the data were collected at 172 points of the study area, and a V_{s30} map of Isparta basin was obtained.

The site classification map of the study area was obtained on the basis of the V_{s30} map according to the seismic codes (NEHRP) that are utilized in the zonation study.

The layers and bedrock variation within the sedimentary deposits accumulated in different geological time such as Holocene, Pleistocene, and Upper Pliocene may be accurately differentiated by using surface wave methods. On the other hand, borehole data may provide significant contribution for interpretation of V_s data. Thus, we used borehole data providing information about the different alluvial units for correlation to V_s map. The borehole data were obtained by compiling logs that have been collected at 33 locations by DSI (18th Regional Directorate, General Directorate of state hydraulic works) for hydrogeological investigations.

2. Geological and tectonic settings

The movement of Anatolian block towards west along the North and the East Anatolian Faults, and the subduction of African plate to Anatolian block along Girit and Cyprus lines are the responsible tectonic elements for the earthquake occurring in the region (McKenzie 1972; Şengör and Yılmaz 1981). Earthquake activity is controlled by Fethiye–Burdur fault zone on the west and Beysehir thrust on the east, which join the Sultandagi Fault on the north of Egirdir Lake and make a triangle shape known as the Isparta Angle (Blumenthal 1963). Isparta basin is located on the north center of the Isparta Angle (figure 1).

The major earthquakes and seismicity of Isparta and surroundings are shown in figure 2 and listed in table 1. Generally, moderate earthquake activity occurs in this tectonic frame. These are as follows. Burdur earthquake ($M_s = 7.0$) occurred on October 04, 1914, and Burdur earthquake ($M_s = 6.2$) occurred on May 12, 1971 (Ambraseys and Finkel 1987; Ambraseys 1988; Taymaz and Price 1992). These earthquakes occurred along Burdur–Fethiye fault zone. It is observed that these earthquakes occurred along the same direction of the fault zone. According to focal mechanism solution, the earthquakes occurred because of normal faulting (Taymaz and Price 1992). Dinar earthquake ($M_s = 6.1$) that occurred on October 01, 1995, caused 10 km faulting (Utkucu *et al.* 2002). Bolvadin (Sultandagı) earthquake ($M_s = 6.0$) occurred on December 15, 2000 (Emre *et al.* 2002; Taymaz *et al.* 2004). Moreover, Çay (Afyon) earthquake that occurred on February 03, 2002, is the most recent large earthquake ($M_w = 6.7$). Çay earthquake occurred near the apex of Isparta Angle (Aktuğ *et al.* 2010). The micro-earthquake map shows that some of the epicenters of the events were located in the Isparta settlement area. These

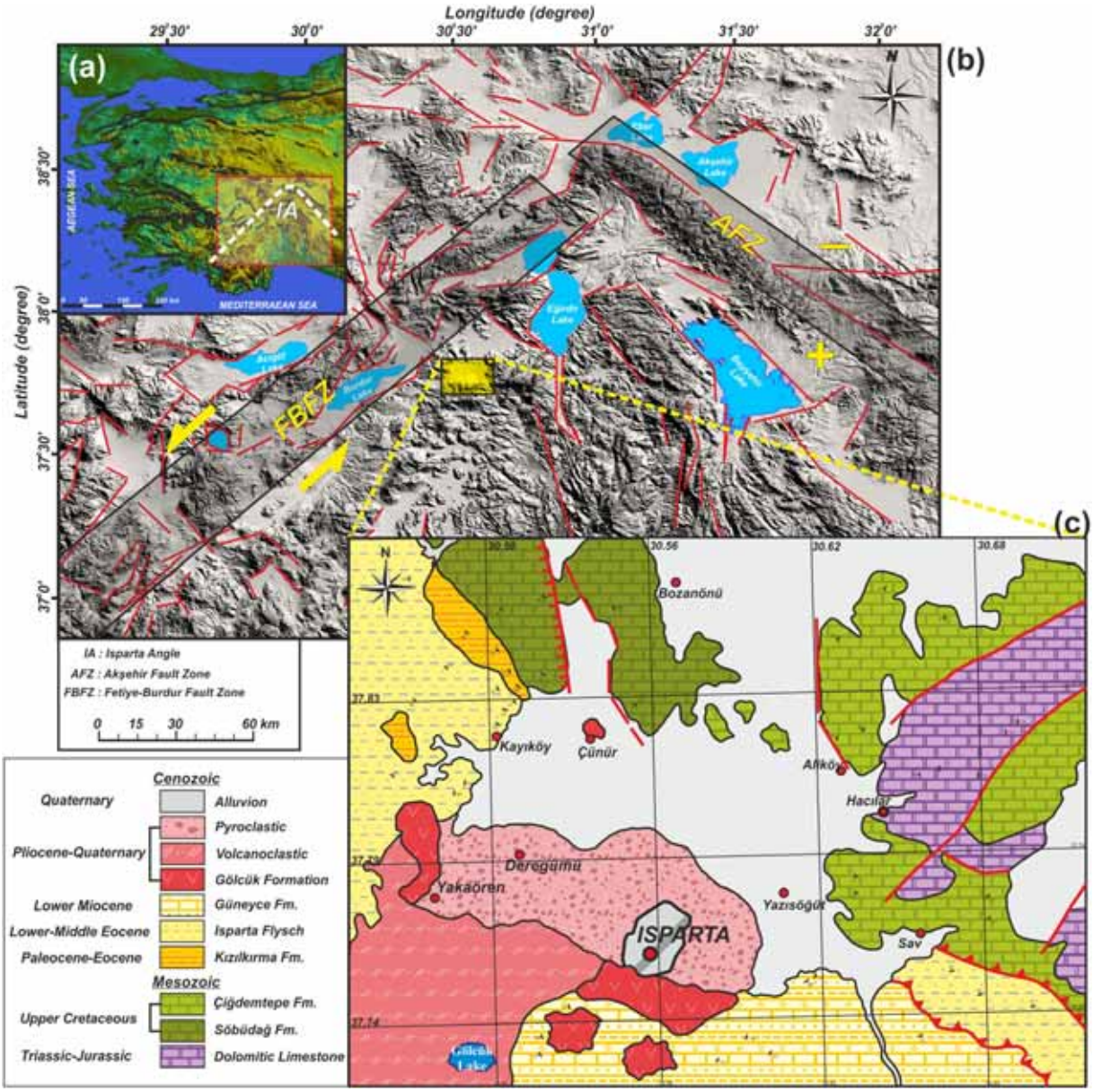

Figure 1. (a) The map of the west Anatolia and Isparta Angle (IA). (b) The map shows tectonics components of IA and study area (modified from Koçyiğit and Deveci (2007)). (c) The map shows geologic units observed in the study area and surroundings.

points correspond to the location of the local faults in the settlement area, which was also mentioned by Koçyiğit and Özacar (2003).

Regional stratigraphic investigations including the study area have been accomplished by a number of scientists (Gutnic and Poisson 1970; Akbulut 1980; Karaman *et al.* 1988; Görmüş and Özkul 1995). According to these studies, the geological features of the investigation area are as follows: Autochthonous Mesozoic Limestone is located at the base of the sequences. Paleogene clastics lay over the Cretaceous units unconformable. Plio-Quaternary rocks are derived from Gölcük Volcanism, and Quaternary terrestrial sediments are the youngest units of the investigation area (figure 1). Upper Cretaceous is represented by thick-layered massif Söbüdağ Limestone and stratified thin-medium-layered Senirce Limestone. Upper Cretaceous Söbü Mount Limestone located at the base of the succession, which is characterized by shallow sea limestone, corresponds to the upper level of Davraz Limestone (Görmüş and Özkul 1995). Deep sea characterized Senirce Limestone (Çiğdemtepe Limestone) overlies conformably on the Söbü Mount Limestone. Kızılkırmak (Koçtepe Fm.) Formation, Isparta Flysch, and Güneyce Formation attributed to the Paleogene overlie uncomfortably on the Upper Cretaceous

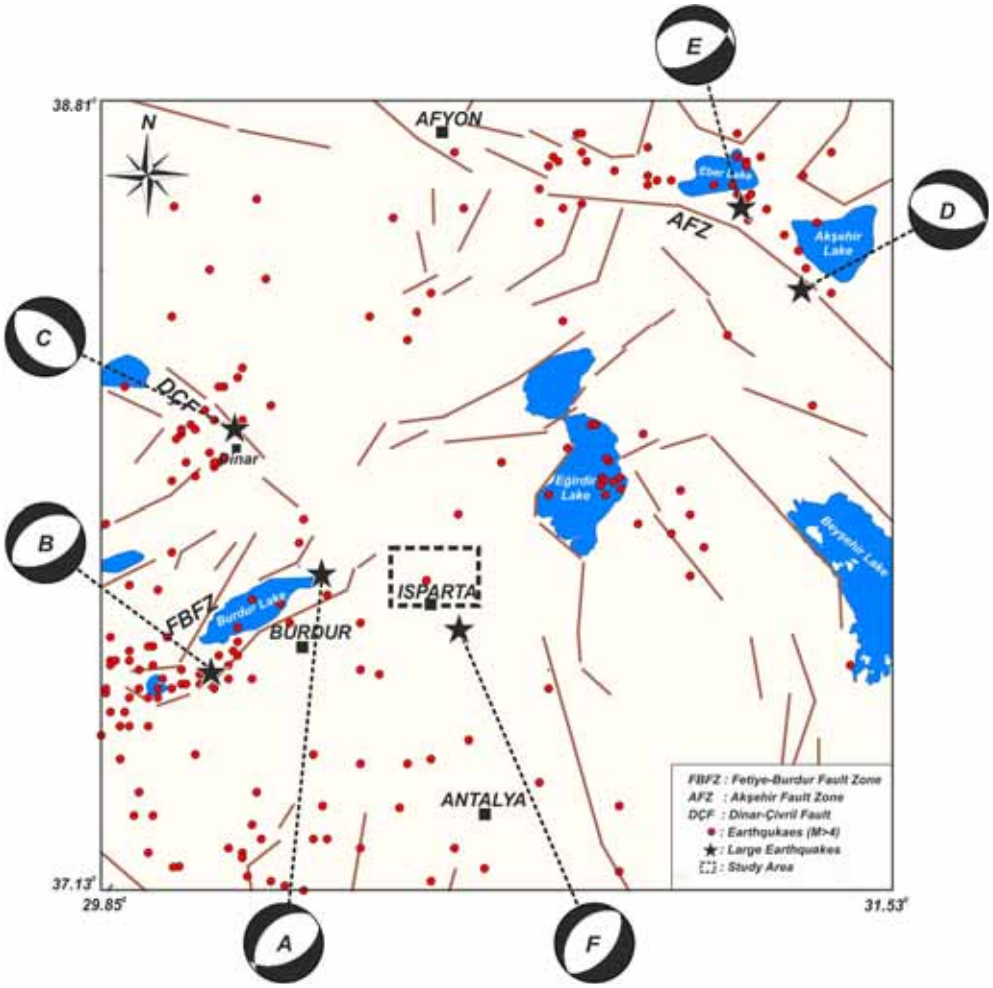

Figure 2. The topographic map of Isparta and surroundings. The map shows fault structures, the major earthquakes shown in table 1, and micro-earthquakes occurred in the area (Kandilli Observatory and Earthquake Research Institute).

Table 1. *The major earthquakes that occurred in the Isparta basin and surroundings.*

No.	Date	Lat.	Long.	Magnitude	Strike°/dip°/ rake°	Reference
A	03.10.1914	37.82	30.27	$M_s = 7.0$	222/42/–107	Ambraseys (1988)
B	12.05.1971	37.64	30.10	$M_s = 6.2$	230/35/–105	Taymaz and Price (1992)
C	01.10.1995	38.105	30.052	$M_s = 6.0$	309/51/–102	Utkucu *et al.* (2002)
D	15.12.2000	38.40	31.33	$M_w = 6.0$	294/40/–80	Taymaz *et al.* (2004)
E	03.02.2002	38.52	31.20	$M_w = 6.2$	258/49/–62	Taymaz *et al.* (2004)
F	24.08.2014	37.683	30.629	$M_w = 5.1$	220/37/–90	USGS

Carbonates (Karaman *et al.* 1988). Upward coarsening Paleogene clastics composed of sequences of sandstone, claystone, marn, and conglomerate represent transition from deep (Kızılkırmak Fm.) to shallow sea (Isparta Flysch and Güneyce Fm.). Trachyandesite, volcanoclastic, and pyroclastic attributed to Plio-Quaternary crop out as dyke at Çünür Hill and at SW of the investigation area. Quaternary alluvium is the youngest unit of the area.

Based on hydrological drillings performed on the Isparta plain, lithology of the accumulated sediments is composed of volcanic block, gravel, sand, silt, and clay (Kanbur *et al.* 2008). Thickness of the frequently sequenced pumice (density: 0.8–0.9 g/cm^3) horizons is between 0.5 and 10 m. Alluvium composed in varying amounts of volcanic block, gravel, sand, silt, and clay is interbedded with the layers of tuff and pumice. It has been observed that these different sized fragments derive from

adjacent Cretaceous limestone and Gölcük trachyandesite.

3. Method

ReMi^{TM} technique has been developed for determining V_s of shallow depth (Louie 2001). It is a passive technique, recording ambient noise or microtremors ubiquitous in the urban environment. V_s is derived by identifying the fundamental mode Rayleigh wave field within the microtremors. This type of data contains lower-frequency in comparison to the bandwidth generated by active sources. Thus, ambient seismic noise is assumed to provide deeper structural information owing to the lower frequency content.

The technique basically requires two steps in practice: data collection and data processing. The data collection is to record the environmental noises due to traffic and other cultural sources linearly over a period of time using standard seismic refraction equipment. This is performed by recording the data using 5–10 m linear arrayed, vertically oriented 4.5 Hz sensors with 12 or 24 channels or more. Maximum depth resolution, as a rule of thumb, can be achieved up to one-third to one-half the length array. Thus, a 230 m array and a 4.5 Hz geophone assures the accuracy of 15% (Pullammanappallil *et al.* 2003).

The data processing contains three steps: velocity spectral analysis, Rayleigh phase-velocity dispersion picking, and shear-wave velocity modelling. This process converts the data records from distance–time (x, t) domain to the slowness-frequency (p, f) domain (McMechan and Yedlin 1981), as described by Louie (2001) and Louie *et al.* (2017). In this manner, the Rayleigh wave is separated from other waves, and the actual phase velocity is determined against the apparent velocity. The scattered Rayleigh wave dispersion curve in p–f spectrum transformed from the recorded wave field can be recognized as high spectral interface. This transformation is particularly effective in allowing accurate picking of Rayleigh-wave phase-velocity dispersion curves despite the presence of waves propagating across the linear

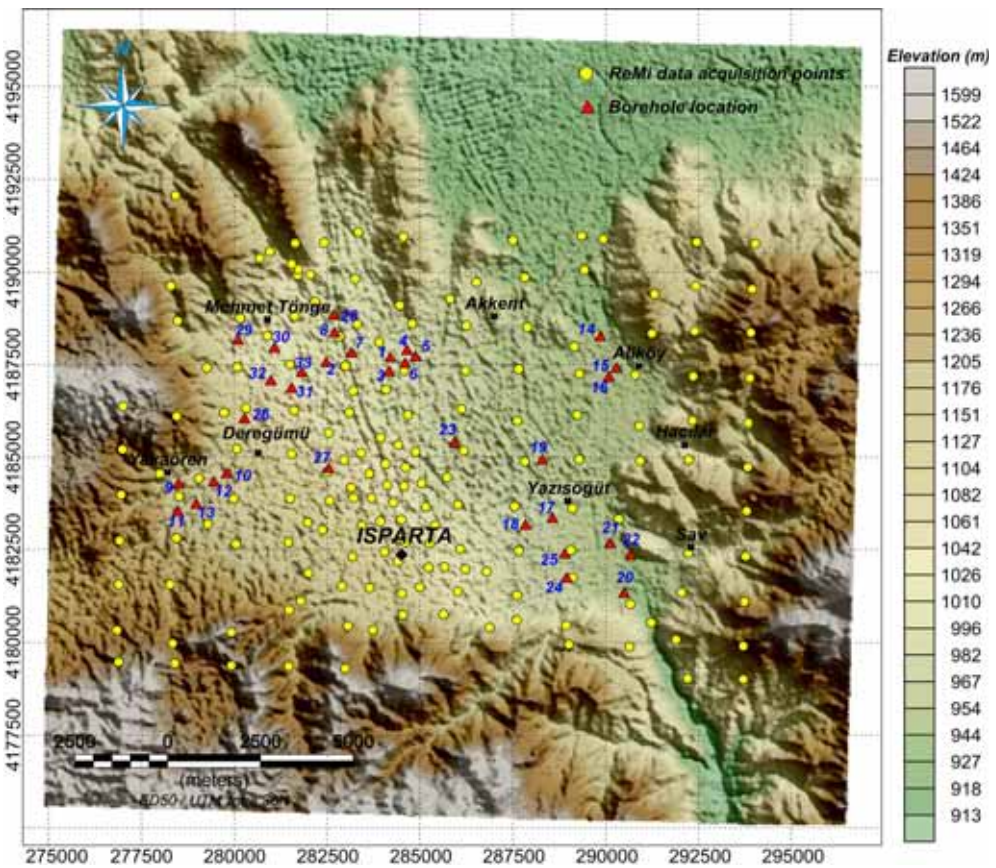

Figure 3. The topographic map of Isparta basin and surrounding shows the distribution of data measurement points (yellow points) and borehole locations (red triangles).

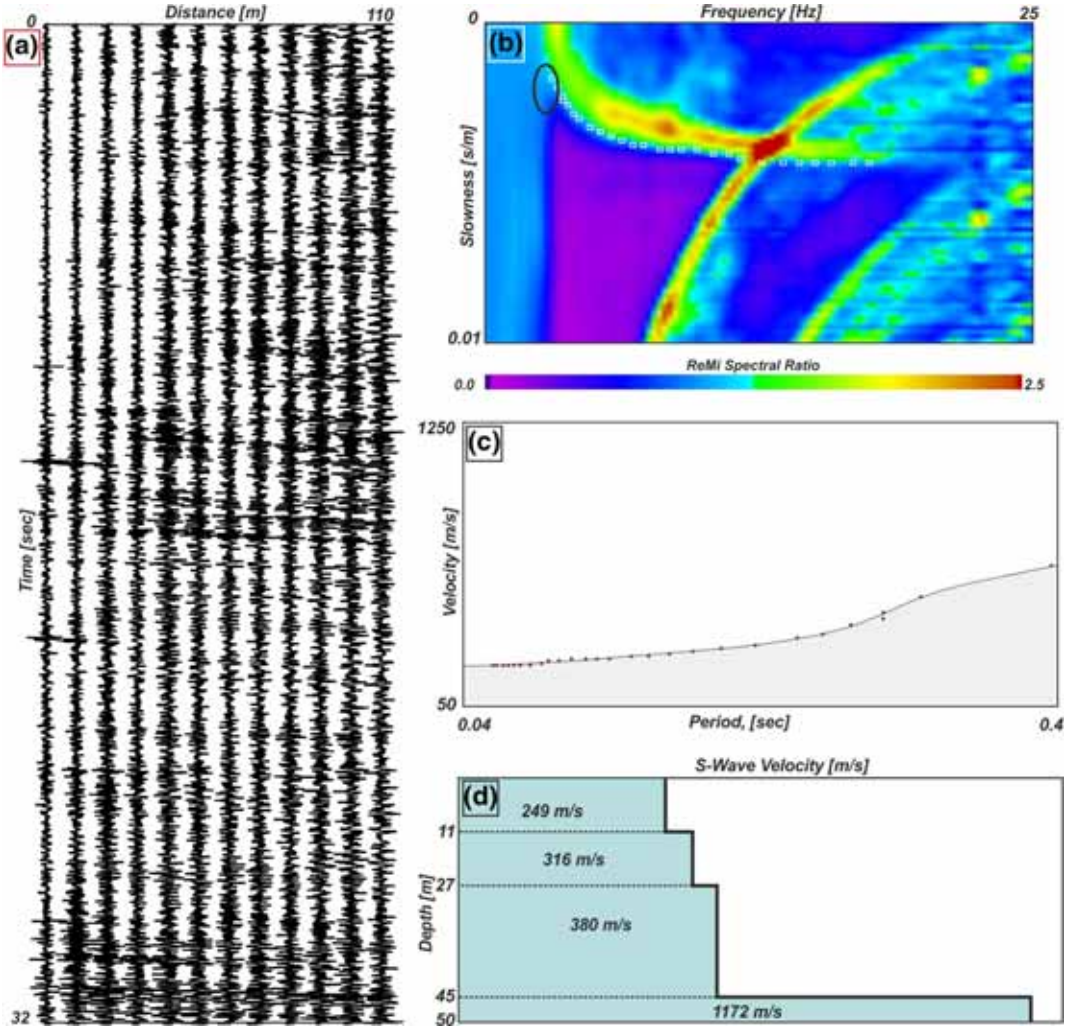

Figure 4. An example of the processed steps of the data. (**a**) the data record in distance–time (x–t) domain, (**b**) the power spectrum in slowness-frequency (p,f) domain calculated from the ambient noise record. Small white boxes were selected on the basis of the average spectral ratio of dispersion curve. (**c**) Measured and theoretically calculated dispersion curves. (**d**) V_s velocities and depths obtained from the theoretically calculated dispersion curve corresponding to the peak dispersion curve shown in white boxes in (b) (V_s modelling was performed for four layers).

array at high apparent velocities, higher mode Rayleigh waves, body waves, air waves, and incoherent noise.

The data record is converted from distance–time (x–t) domain to ray parameter (inverse of the apparent velocity)–intercept time (p–τ) domain as described by Thorson and Claerbout (1985) and the detailed mathematical expression is given in Louie (2001). Then, the data are transformed from the p–τ domain to the p–f domain by Fourier transform, as shown by McMechan and Yedlin (1981). This is performed by Fourier transformation as the calculated each (p, τ) trace in the direction of τ-axis. After the successive application of the power spectrum (p–f), which is the magnitude squared of the complex Fourier transform as described in Louie (2001), the conversion of seismic record is completed.

After the dispersion curve is obtained from the p–f spectrum, it may be modelled to determine the subsurface V_s structures. This can be performed by forward or inverse modelling. The borehole data may be useful for determining the beginning of the number of layers used in velocity–depth modelling. If there is no such data in a location, the modelling is started by minimum number of layers to produce a best velocity structure (Pancha *et al.* 2017b). The interactive forward solutions commercial software package (SeisOpt ReMi^{TM}, Optim (2006)), which is based on code of Saito (1979, 1988), was used for modelling. The analysis and modelling methodology

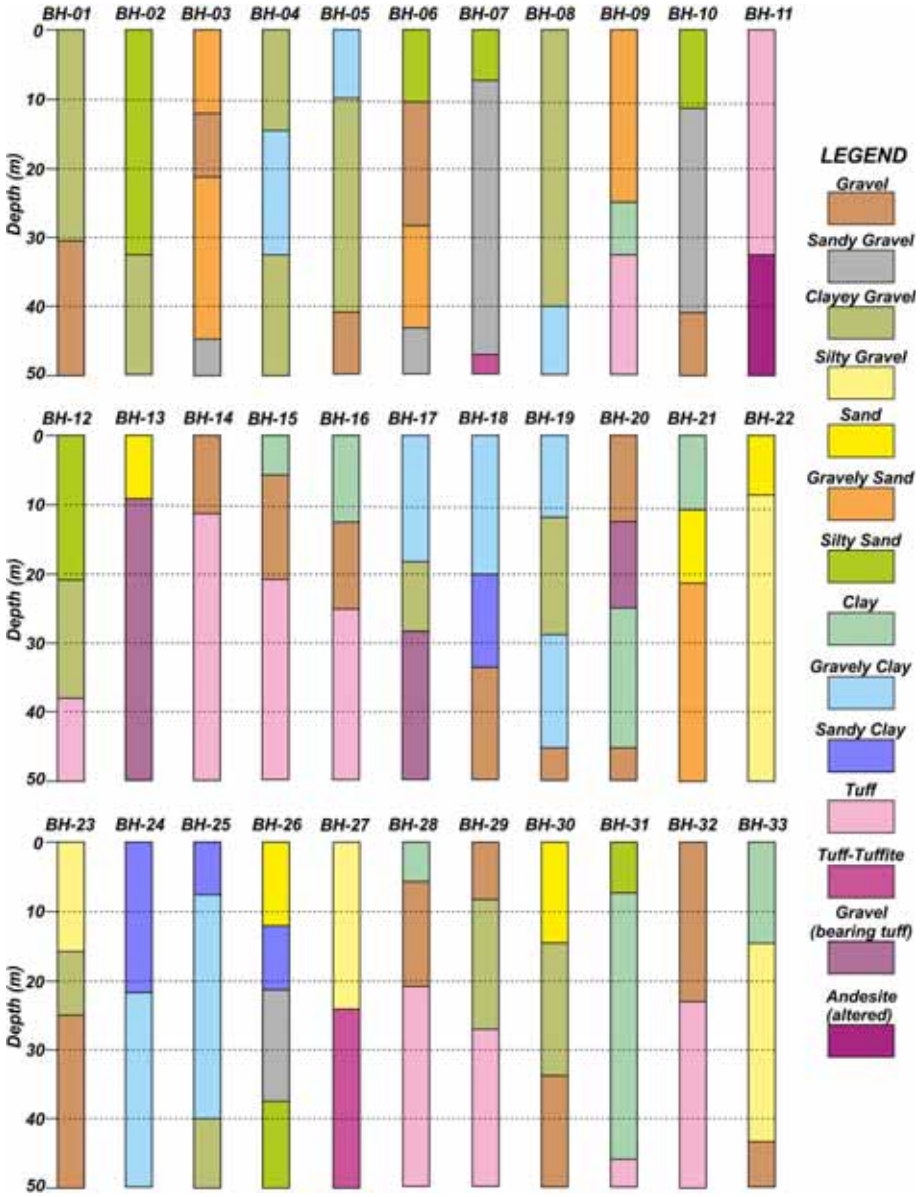

Figure 5. The borehole lithology at different depth levels. (**a**) 5 m depth, (**b**) 15 m depth, (**c**) 30 m depth, and (**d**) 50 m depth. (The borehole database was constructed by compiling borehole logs, which were conducted by DSI (18th Regional Directorate, General Directorate of state hydraulic works).

was described by Louie (2001) and Louie *et al.* (2017) in detail.

4. Data acquisition and processing

A 12-channel engineering seismography and 4.5 Hz vertical geophones were used in this study. The natural frequency of the geophones used depends on the target depth because the depth penetration is inversely proportional to the geophone frequency. Furthermore, the x and t dimensions vary according to the depth of the target. A 110 m array length and use of 4.5-Hz geophones will allow the V_s modelling up to 50 m depth. A channel interval of 10 m and a recording time of 32 ms with a sampling interval of 2 ms were used. To increase the spectral ratio, 10 records were acquired at each station. The main roads where traffic may be intense in the study area were preferred for better data collection. As a result, the data were collected at the 172 points in Isparta and surroundings, as shown in figure 3.

The character and quality of each acquired dispersion image vary according to the transient ambient noise recorded for a given site. A sample record is shown in figure 4(a). We have 10 data records at each site. After p–f transformation was

Table 2. *The table shows the location of data measurement points, V_{s30}, site classification and modelling error (m/s).*

Data acq. point	Longitude (UTM-WGS84)	Latitude (UTM-WGS84)	V_{s30} (m/s)	Modelling error (m/s)	NEHRP site class
1	277985	4184556	480	9.27	C
2	285152	4183659	392	5.58	C
3	278269	4181564	342	10.25	D
4	278441	4182816	334	12.47	D
5	278513	4183947	452	10.73	C
6	279044	4184426	407	7.69	C
7	279264	4187414	373	8.73	C
8	279729	4186200	442	7.59	C
9	280084	4187425	346	4.29	D
10	280156	4188751	1215	10.82	B
11	280687	4190356	1366	6.27	B
12	280314	4186324	360	5.17	C
13	280066	4185230	412	12.07	C
14	279986	4183882	327	5.73	D
15	279287	4183190	343	7.69	D
16	280043	4182656	377	8.62	C
17	281477	4180875	490	6.38	C
18	281789	4181112	334	9.12	D
19	281995	4181870	363	8.95	C
20	281460	4182704	347	8.71	D
21	291896	4180077	1177	10.30	B
22	290640	4179886	1205	9.62	B
23	289012	4179948	1299	8.23	B
24	281540	4185086	298	5.49	D
25	282540	4185652	350	10.59	D
26	281607	4186258	314	7.40	D
27	281499	4187497	386	4.23	C
28	280886	4188273	313	6.75	D
29	281620	4188807	312	4.48	D
30	282176	4189196	409	7.82	C
31	282048	4189932	439	8.14	C
32	281706	4189911	663	8.22	C
33	281724	4190071	683	10.32	C
34	281544	4190206	1127	10.65	B
35	280959	4190545	481	9.85	C
36	278448	4186103	1034	11.22	B
37	283252	4189818	334	9.10	D
38	283316	4188588	398	10.95	C
39	283896	4188102	391	7.58	C
40	282993	4187456	284	6.85	D
41	283096	4186199	313	7.98	D
42	284085	4186821	308	2.80	D
43	283183	4182312	342	7.74	D
44	283730	4180339	399	12.7	C
45	284540	4180750	436	9.02	C
46	284512	4181313	328	11.07	D
47	284406	4182182	369	8.34	C
48	284995	4181491	326	7.84	D
49	284611	4182702	338	7.06	D
50	285260	4182677	417	8.11	C
51	285663	4182035	366	10.83	C
52	286179	4185175	384	7.85	C
53	286120	4186293	507	12.05	C

Table 2. *(Continued.)*

Data acq. point	Longitude (UTM-WGS84)	Latitude (UTM-WGS84)	V_{s30} (m/s)	Modelling error (m/s)	NEHRP site class
54	286230	4187332	312	8.44	D
55	286249	4188552	341	6.83	D
56	285812	4189274	569	7.94	C
57	284672	4186141	291	8.91	D
58	284578	4187332	290	7.41	D
59	284786	4188602	763	13.71	B
60	286520	4189719	345	6.13	D
61	286873	4180409	468	9.37	C
62	287604	4180607	426	4.64	C
63	287613	4181272	356	8.01	D
64	287667	4182472	349	11.44	D
65	287550	4183669	312	7.71	D
66	287821	4184882	297	7.66	D
67	287619	4185978	304	5.91	D
68	287661	4187375	283	5.93	D
69	287895	4188509	606	4.72	C
70	287825	4189856	292	5.58	D
71	287503	4190846	273	6.60	D
72	289156	4187986	787	12.73	B
73	289108	4183617	342	8.51	D
74	289066	4182489	458	8.16	C
75	289109	4181741	510	6.50	C
76	288942	4180462	623	8.28	C
77	291226	4180538	546	5.68	C
78	290664	4181029	357	7.66	D
79	292045	4181345	655	4.12	C
80	290690	4182305	342	5.68	D
81	292227	4182407	384	10.18	C
82	290353	4183329	343	7.63	D
83	293841	4185922	1448	12.75	B
84	293887	4187136	1473	10.68	B
85	290928	4184903	648	11.53	C
86	290910	4185842	369	5.19	C
87	292238	4184932	674	12.03	C
88	290799	4187214	441	5.80	C
89	287020	4188854	1096	8.08	B
90	284069	4184825	383	11.30	C
91	284879	4185145	287	6.81	D
92	284412	4185334	372	11.25	C
93	283938	4185524	306	8.54	D
94	284454	4189097	894	10.76	B
95	283413	4185119	342	12.08	D
96	282954	4184926	368	8.50	C
97	283638	4184557	361	4.01	C
98	283148	4184179	401	5.31	C
99	283207	4183900	334	4.11	D
100	284118	4184248	367	6.25	C
101	283692	4183900	407	5.90	C
102	284284	4183776	386	5.10	C
103	283932	4183269	369	4.78	C
104	283436	4183153	411	6.06	C
105	284498	4183310	341	4.30	D
106	278341	4179977	476	11.15	C

Table 2. *(Continued.)*

Data acq. point	Longitude (UTM-WGS84)	Latitude (UTM-WGS84)	V_{s30} (m/s)	Modelling error (m/s)	NEHRP site class
107	285042	4184294	299	7.00	D
108	284608	4184728	435	6.14	C
109	284575	4184223	375	5.88	C
110	285404	4183162	342	7.36	D
111	286796	4181911	346	6.76	D
112	282418	4190783	377	9.44	C
113	282832	4188260	337	7.34	D
114	283199	4186793	304	6.90	D
115	285233	4182020	361	8.40	C
116	286215	4181975	381	7.78	C
117	285728	4184456	350	4.13	D
118	281974	4183234	381	8.44	C
119	283345	4191069	254	6.54	D
120	278477	4188679	1364	8.95	B
121	278290	4189621	1396	7.71	B
122	278418	4192064	1322	6.81	B
123	282374	4183039	389	10.74	C
124	281505	4183884	400	9.19	C
125	282573	4183832	331	10.40	D
126	282498	4184600	344	9.68	D
127	284553	4190945	888	8.66	B
128	281640	4190771	1127	12.59	B
129	291317	4189403	1150	10.01	B
130	291247	4188335	1112	7.27	B
131	289295	4187247	338	6.97	D
132	289231	4186137	358	7.31	D
133	289285	4184943	421	5.61	C
134	277001	4186368	1237	12.69	B
135	276984	4185209	949	9.33	B
136	276955	4183991	903	7.23	B
137	276909	4182746	1152	10.96	B
138	285634	4180763	368	11.44	C
139	286018	4181374	373	8.52	C
140	286083	4182520	367	7.96	C
141	286021	4183714	277	5.70	D
142	276892	4181563	771	7.12	B
143	276842	4180336	1034	12.60	B
144	276882	4179472	1328	11.45	B
145	278399	4179438	501	6.32	C
146	279920	4180277	1421	12.17	B
147	279918	4179379	1277	12.86	B
148	281464	4179359	544	6.96	C
149	282983	4179299	1546	13.01	A
150	292455	4190799	528	7.25	C
151	292429	4189621	421	8.44	C
152	292396	4188399	1225	9.86	B
153	292359	4187177	1177	12.14	B
154	292341	4185983	1106	7.42	B
155	292204	4179030	1059	9.66	B
156	289355	4190967	329	5.62	D
157	289431	4190049	343	6.60	D
158	289934	4190878	411	8.69	C
159	289797	4188287	361	7.79	C

Table 2. *(Continued.)*

Data acq. point	Longitude (UTM-WGS84)	Latitude (UTM-WGS84)	V_{s30} (m/s)	Modelling error (m/s)	NEHRP site class
160	293708	4179005	1397	12.13	B
161	293705	4179903	1613	13.8	A
162	293737	4181095	1076	12.45	B
163	293774	4182322	1042	8.69	B
164	293799	4183544	1483	10.12	B
165	293827	4184732	1460	12.64	B
166	282893	4181517	300	9.09	D
167	284043	4182448	460	8.31	C
168	283645	4181471	412	11.47	C
169	283057	4180447	459	11.29	C
170	293912	4188360	1215	9.63	B
171	293945	4189534	565	7.67	C
172	294027	4190756	550	6.16	C

applied to each record, p–f images were obtained corresponding to each record. The p–f images were stacked, and a final enhanced p–f image was obtained. The power spectrum of this record is shown in figure 4(b). The best suitable place to select the dispersion curve from the power spectrum is the light green and light blue interface, which provides the highest power spectral ratio. The narrower light green and light blue interface provides less ambiguity in seismic velocity–depth model. At shallow depths, this interface appears to be quite narrow. This leads to the correct calculation of V_{s30}. However, for the deeper depths toward the end of the spectrum (shown by ellipse in figure 4b), this interface may be larger, depending on the maximum offset of seismic array and depth relationship, which increases uncertainty. The reliability of the velocity and depths to be calculated, especially for the deeper values, depends on the fact that the picks to be selected are from this area. Therefore, the picks should be selected from the less uncertainty area as possible. ReMi^{TM} arrays in this study used 4.5 Hz geophones, thereby constraining the dispersion curve analysis to frequencies below 3 Hz (Odum *et al.* 2013). Finally, the dispersion curve is obtained as high spectral ratio from the spectrum (figure 4c).

The subsurface V_s information from the obtained dispersion curve in the p–f spectrum may be modelled by the commercial software ReMi^{TM} interactive forward solutions package. The Shear velocity–depth (V_s –z) modelling is simply done by iterating on phase velocity, layer thicknesses, and a number of layers in the model until finding the reasonable solution within the iteration parameters. The interactive modelling code does not require any specific initial model. However, the modelling may be simplified in the light of the stratigraphic column of the study area. Geological map of the study area shows that the stratigraphic component is simply listed from bottom to surface as Sobu mount limestone, the Flysch (Isparta formation), slope, and alluvial deposits. We also compiled the available borehole data acquired in the Isparta alluvial basin as initial information and to compare the distribution of seismic V_s values. A total of 33 borehole records were obtained from the reports of DSI. The depth of the boreholes varies from 50 m to 250 m. The distribution of boreholes in the basin is shown in figure 3. From the borehole distribution, the alluvial basin consists of four major geological units as sand, clay, gravel, and tuff–tuffite (figure 5). V_s–z profile modelled from a data record may be used as an initial model for the other data collected at close locations having similar geology. It is expected that only a slight change in the modelling of data records unless a dramatic lateral change takes place. Thus, the successively obtained previous model may use an initial model for the next data record. The best fit between the observed dispersion picks and the theoretical model dispersion curve is the final model that is generally appeared with the lowest rms error value less than %5 by using the fewest layers. The V_s –z models were generated using the fundamental mode of Rayleigh wave. Figure 4(d) shows the 1D V_s–z structure obtained by modelling the dispersion curve shown in figure 4. The data processing was completed by modelling all data records one by one.

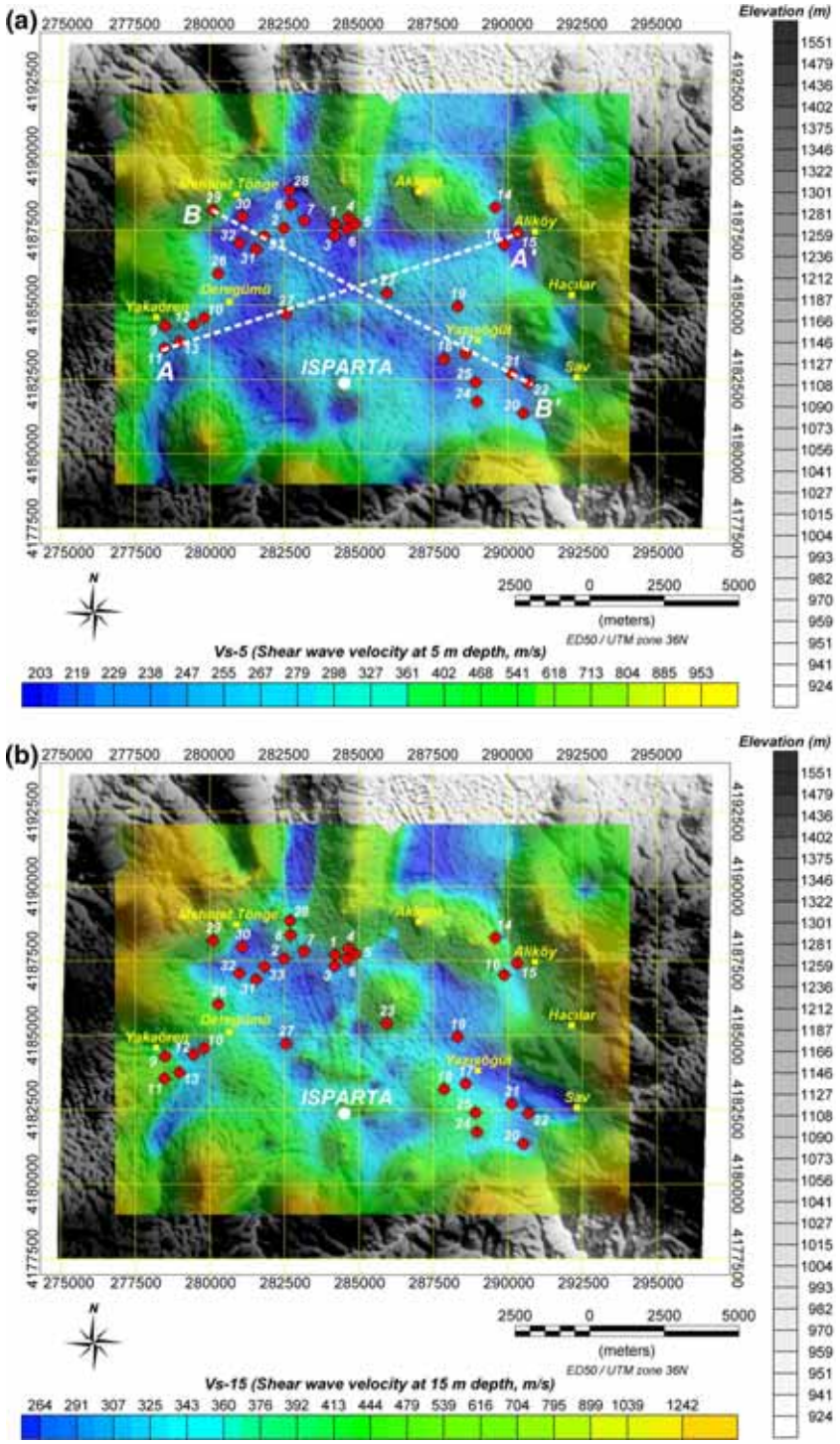

Figure 6. Map shows V_s distribution at Isparta basin and surrounding at 5 (**a**) and 15 m (**b**) depths.

4.1 *Uncertainty*

The array length and depth resolution achievement and modelling the data by forward solution may result in uncertainty. A 110 m array length would allow the V_s modelling up to 50 m depth according to the rule of thumb, can be achieved up to one-third to one-half the length array. This may be achieved by recording very low-frequency noise using low-frequency geophones (4.5 Hz) (Pullammanappallil *et al.* 2003). In the p–f spectrum, the dispersion curve should appear around the minimum-velocity envelope at the base of the high spectral ratios as Louie (2001) and Louie *et al.* (2017) describes. It is represented by the light green and light blue interface in the p–f spectrum,

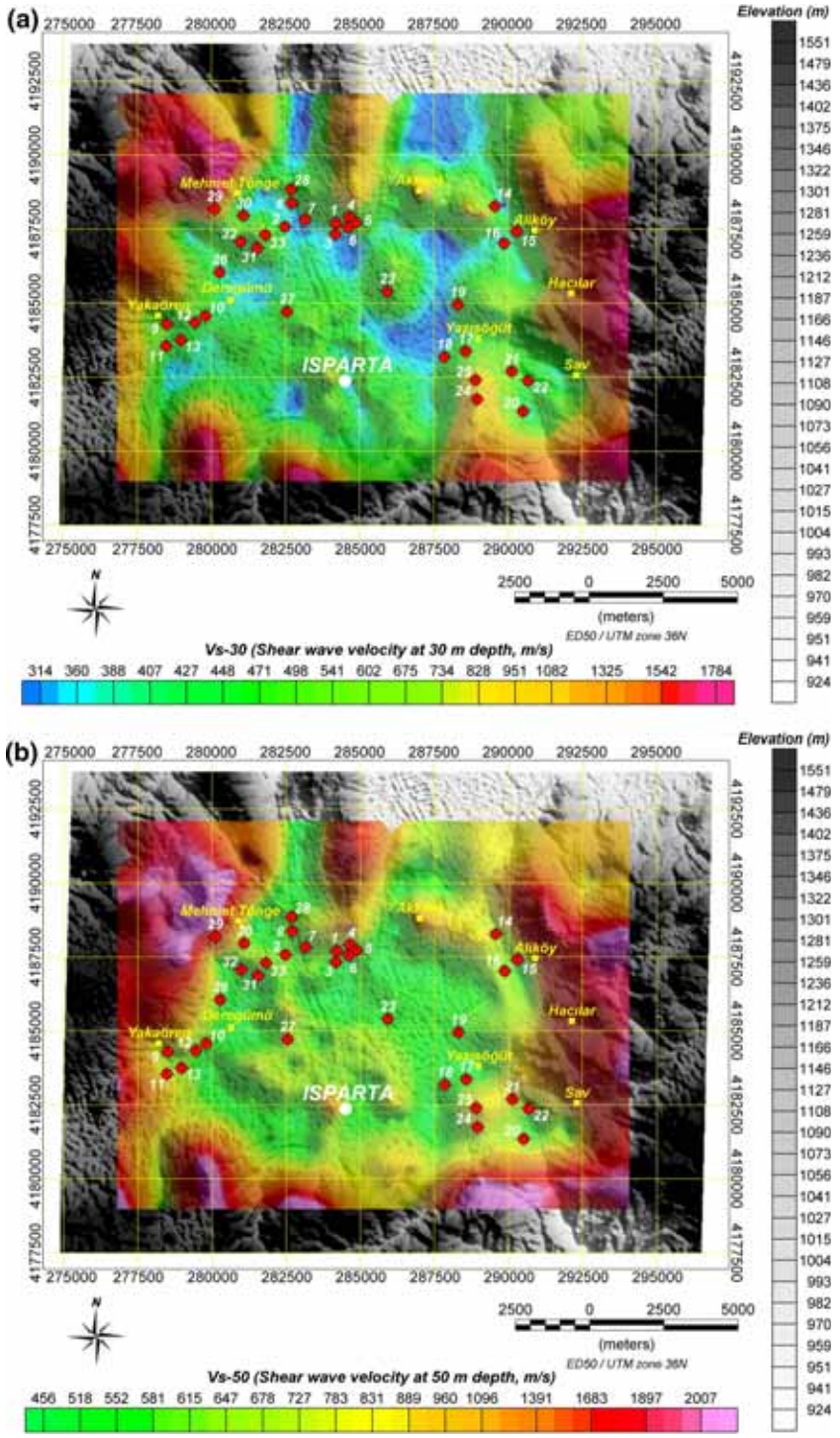

Figure 7. Map shows V_s distribution at Isparta basin and surrounding at 30 (**a**) and 50 m (**b**) depths.

appearing clearly between 3.5 and 12 Hz in figure 4(b), providing less uncertainty in the model. The deeper part (below 3.5 Hz) of the spectrum (shown by an ellipse in figure 4b) shows the p–f artifacts resulting in more uncertainty. The last picks (shown by the white box) appear between 3 and 3.5 Hz corresponding the velocity 450–560 m/s, which results in (±55 m/s) %10 error.

Forward or inversion solution of the dispersion curves provide a one-dimensional shear-wave velocity (V_s) models down to a depth related to the length of the array. Due to the non-uniqueness of the solution, complementary information such as borehole data may give a significant contribution to modelling. The distribution of boreholes in the basin (figure 3) as the initial information was taken

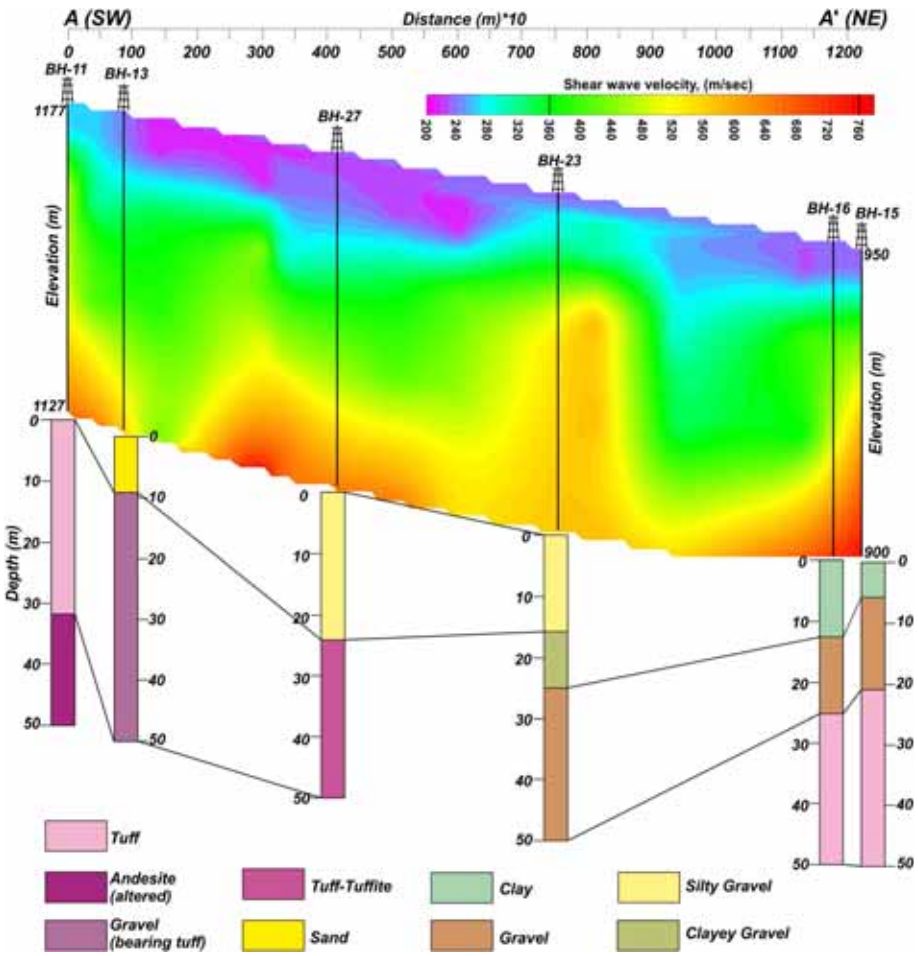

Figure 8. The comparison of the selected borehole records and V_s velocities along the AA′ cross-section. The locations are shown in figure 6(a).

into account during the V_s–z modelling process. The major geological units encountered in the study area may provide to staying in a more reliable initial model for modelling. In overall, the selected dispersion picks can control the trade-off between the depth and velocity of this interface up to 3.5 Hz, showing that the model could match the dispersion picks with the low modelling error. The depth and the velocity of the deeper layer increases non-uniqueness and may be determined between 3 and 3.5 Hz with the higher modelling error. Table 2 shows the V_s structure of all data and the modelling of the dispersion error varying between 4 and 13%.

5. Results and interpretation

All the data records were converted to 1D velocity–depth models and mapped. To observe the change in the sedimentary units by depth, the shear-wave velocity maps for various depths were generated. Before creating the map of soil classification, which was based on V_{s30} values, the shear velocities were mapped at 5, 15, 30, and 50 m depth levels, respectively, as shown in figures 6 and 7. In addition, the geological units in the borehole records are also classified based on 5, 15, 30 and 50 m depths, as shown in figure 5.

Figure 6(a) shows the V_s map at 5 m depth. In the basin, the V_s velocity appears as mostly blue tones in the range from 203 to 950 m/s. It is observed that the V_s values are highly affected by the near surface low-velocity layers at this depth, particularly the outer parts of the basin. The borehole record in figure 5 shows that clay and sand are the dominant geological units at this depth. Figure 6(b) shows the V_s map at 15 m depth. The V_s velocity appears as mostly green tones in the range from 264 to 1242 m/s. At the outer part of the basin, the velocity is affected by rock units rather than alluvium. Even though the loose clay and sand are also dominant units in the basin at this depth, the relatively higher gravel

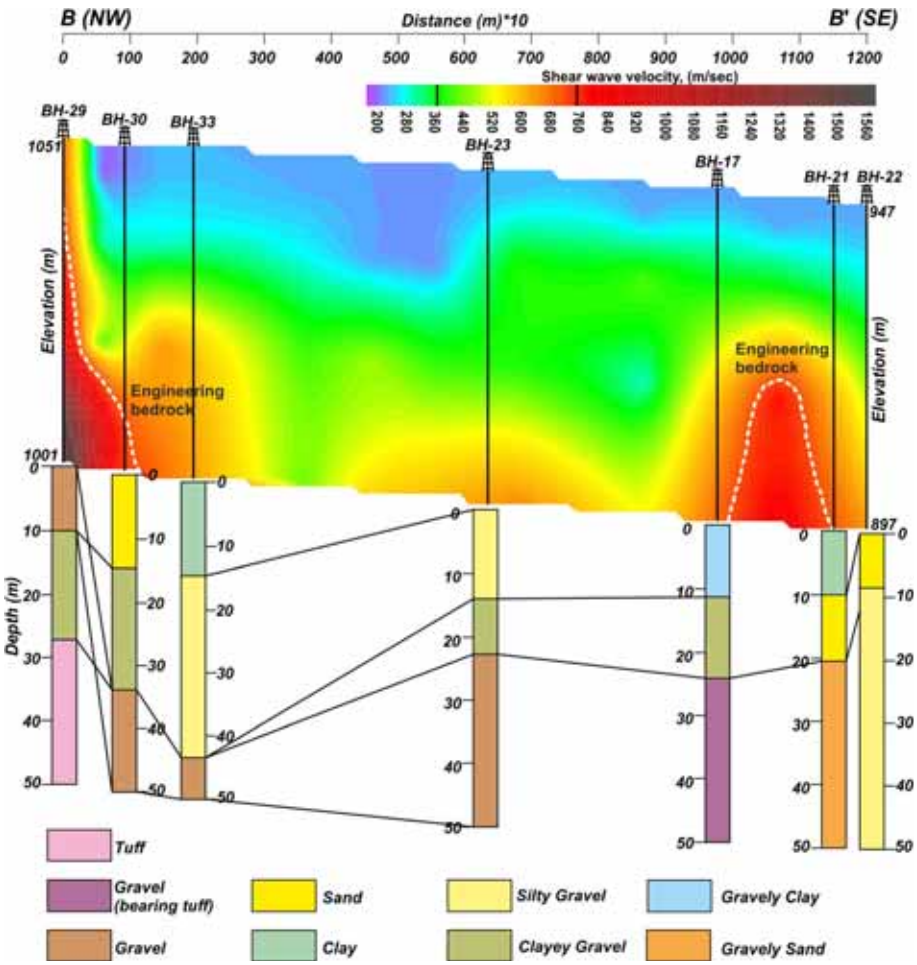

Figure 9. The comparison of the selected borehole records and V_s velocities along the BB′ cross-section. The locations are shown in figure 6(a).

content should be responsible from the higher V_s. Figure 7(a) shows the V_s map at 30 m depth. The V_s velocity appears as almost entirely green tones in the range of 314–1784 m/s. Figure 7(b) shows the V_s map at 50 m depth. The V_s velocity appears as green and yellow tones in the range from 456 to 2007 m/s. Figure 5 shows that the more gravel and the existing tuff, tuffite and andesite contents should be the primary reason for the higher velocities at these depths. The maps show (figures 6 and 7) that the velocity gradually increases with the depth. However, as seen from figure 5, lateral variations are also existed. This result shows that the similar depositional of sedimentations sometimes may show significant variations at different locations.

The alluvial deposits of the basin contain both fine and coarse grained materials and volcanoclastic such as tuff, tuffite, and andesite deposition. V_s velocities and borehole data were compared along A–A′ and B–B′ cross-sections that are close to many borehole points along the lines (see location of cross-sections in figure 6a). The cross-sections are shown in figures 8 and 9, respectively. Three main velocity structures are evident in the cross-sections. These are represented by pink-light blue, green, and yellow-red colors, which are corresponding the range of <300 m/s, 300–500 m/s, and >500, respectively. The contents of the first velocity structure as surface material consists of mostly one of the units of sand, silt, and clay or all and emerge the V_s below 300 m/s. The second velocity structure, which is underlying this group, differs by mixing the units of gravel, tuff, and andesite to the units of sand, silt, and clay and emerge the V_s between 300 and 500 m/s. The third velocity structure consists of mostly one of the units of gravel, tuff, and andesite or all and emerge the V_s above 500 m/s. It can be observed that the coarse grained materials and volcanoclastic are the main factors that increase the seismic velocity. The V_s values of these units exceed 500 m/s at 50 m

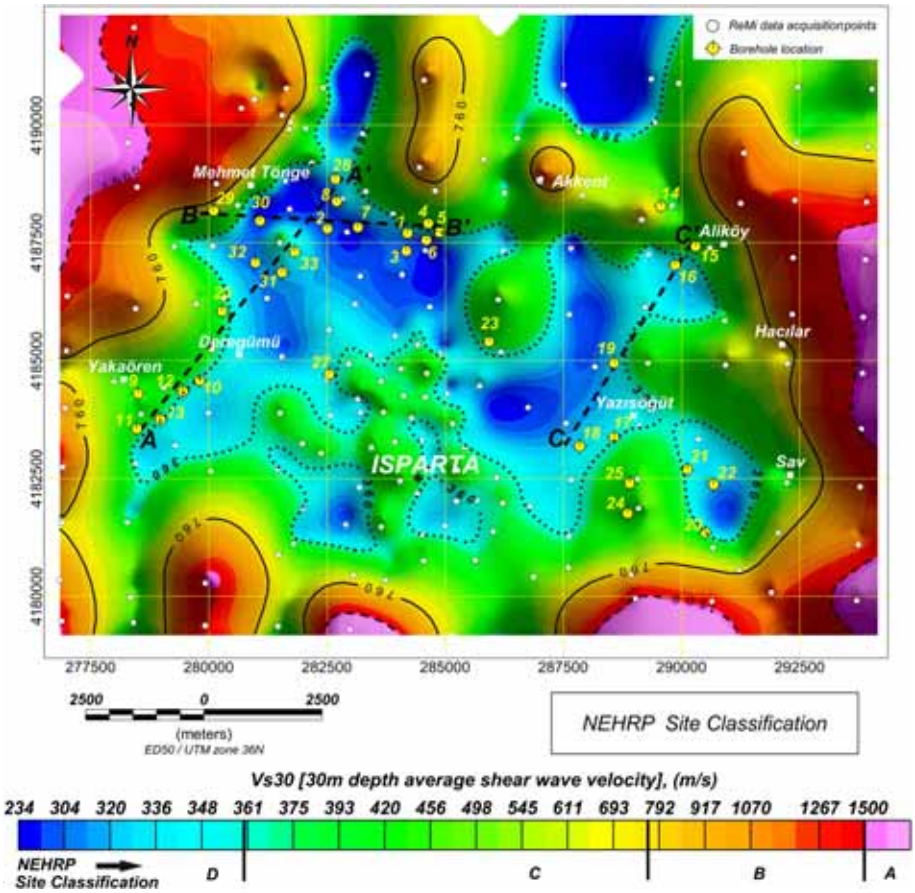

Figure 10. V_{s30} and NEHRP site classification map of Isparta basin and surrounding area.

depth. Under the control of the axial deposition system, the V_s velocity of the alluvium deposits of the basin gradually increases with depth. However, a strong velocity change is observed especially when the lithology changes as from the alluvial deposit to the fluvial-clay, silty-clay, and clayey-silt deposits.

The average shear-wave velocity of the upper 30 m of a soil profile (V_{s30}) is an important indicator for site response. Borcherdt (1994) suggest that the uppermost 30 m is the key part for the site classification based on the effects of the soil types related with ground motion response. Anderson *et al.* (1996) also interpreted the use of the average shear-wave velocity in the upper 30 m and showed that attenuation affects ground motions as much as shear velocity. V_{s30} values are computed from the layers V_s velocity within upper 30 m depth according to equation (1) for classifying the sites based on the NEHRP. Site classification distribution map of Isparta was created according to NEHRP criteria.

According to the NEHRP criteria, V_s of the subsurface must be measured to depth of 30 m. Soil profiles, which may contain different soil layers are subdivided into the layers that may be represented by 'n' distinct layers in the upper 30 m. The V_s values assigned to the subsurface at a specific site is calculated using equation (1) and so that V_{s30} is obtained.

$$V_s = \frac{\sum_{i=1}^{n} d_i}{\sum_{i=1}^{n} \frac{d_i}{V_{si}}}. \quad (1)$$

Here, total thickness of the soil profile is equal to 30 m. i refers to one of the layers between 1 and n, V_s refers to shear-wave velocity (m/s) and d_i is the layer thickness between 0 and 30 m.

V_{s30} values of each V_s–z model were calculated by using equation (1) and V_{s30} map was obtained. Finally, the site classification zonation map of the study was obtained by using V_{s30} according to NEHRP criteria (BSSC 2003). Figure 10 shows V_{s30} and site classification map.

2D maps were created using the lithologic units obtained from the irregularly distributed borehole records over the study area (figures 11, 12, 13). This maps provides to compare the V_{s30} and

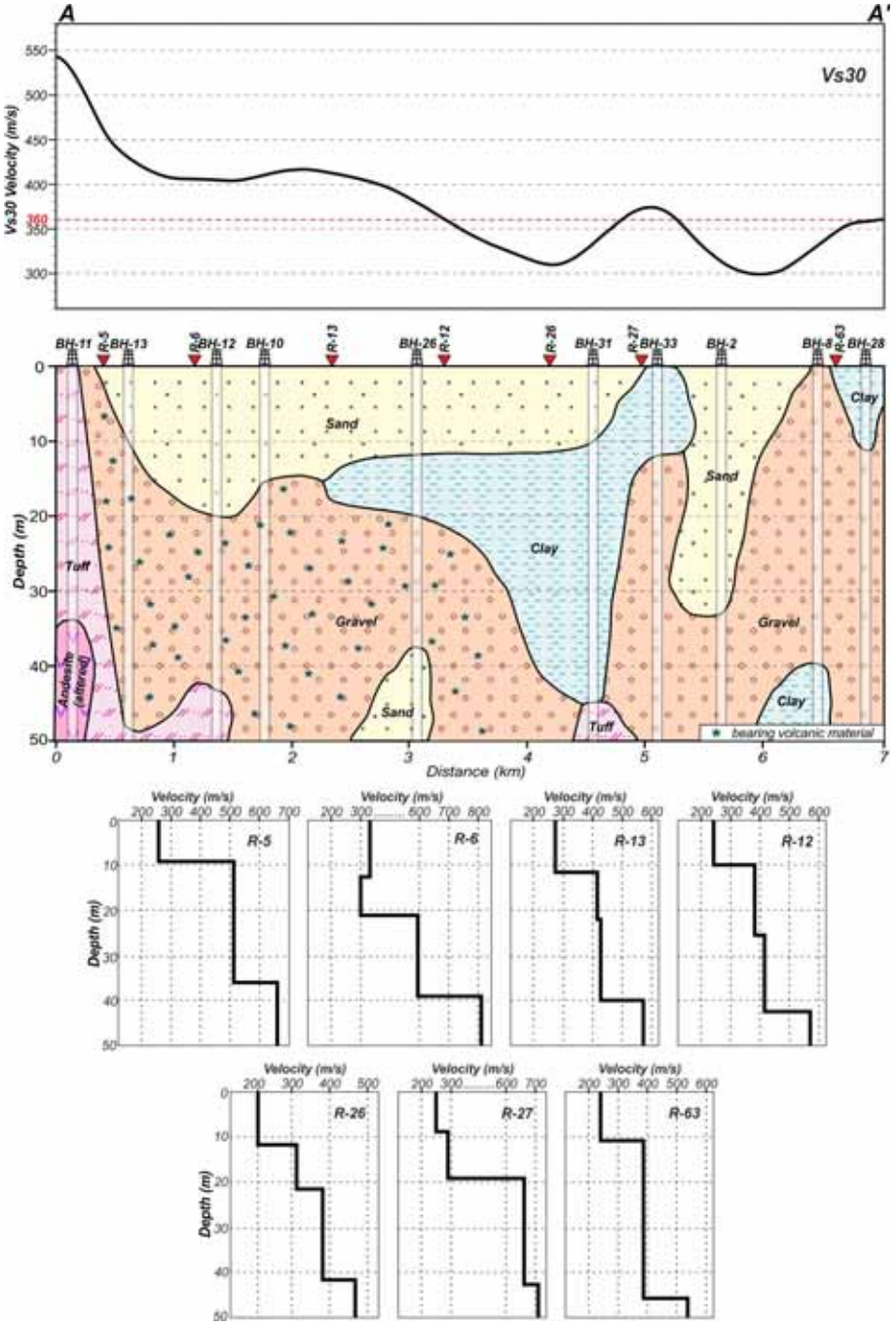

Figure 11. 2D cross-section of basin sediments the along the profile A–A′. The location is shown in figure 10. (Top panel) V_{s30} curve, (middle panel) geological cross-section, (bottom panel) 1D V_s-depth models at the borehole points.

classification map to the lithology of the basin. The comparison showed that three main lithological group emerged as sand-clay, gravel, and tuff–tuffite.

The map of V_{s30} shows that the velocities emerge generally in the range of 203–1600 m/s. The V_s of sediments generally increases with depth and geological age. Singh *et al.* (2017) presented a good example of the correlation between V_s depth and geological age. While we determine velocity levels with depth, we also indicated the corresponding geological age from the map as well as V_s and lithological ages. It can be seen that the alluvial basin emerged at relatively low seismic velocities (200–450 m/s). The velocity is gradually increased due to the influence of the pyroclastic rocks formed by the volcanism of Gölcük in this area towards the southern part of the basin. 760 m/s and higher velocities corresponding B and A group soil are the rocks according to NEHRP. These soil classes

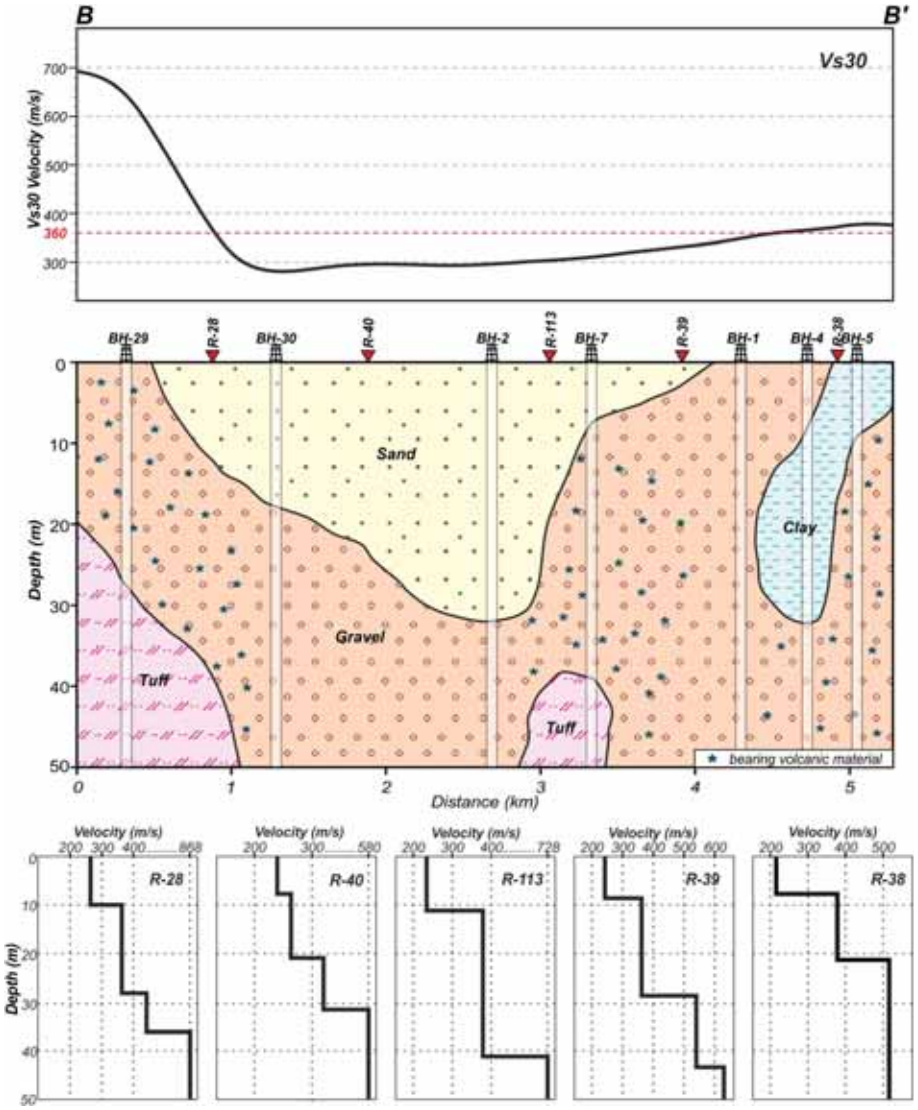

Figure 12. 2D cross-section of basin sediments the along the profile B–B′. The location is shown in figure 10. (Top panel) V_{s30} curve, (middle panel) geological cross-section, (bottom panel) 1D V_s-depth models at the borehole points.

correspond to the part of the study area emerged on the outer side of the basin. All the rocks emerged in this area (figure 1) such as Cenozoic and Mesozoic formations except Pyroclastic and alluvium constitute A and B soil types (figure 10). V_{s30} values between 360 and 760 m/s corresponds to soil class C according to NEHRP. The site C class encompasses both the Quaternary and Pliocene sediments towards the edge of the basin. V_{s30} between 180 and 360 m/s corresponds to soil class D according to NEHRP. The alluvium basin sediments comprise mostly plain and little slope deposits.

The alluvial deposits contain both fine coarse grained materials and volcanoclastic such as tuff, tuffite, and andesite depositions. The coarse grained materials and volcanoclastic are the main factors that increases the seismic velocity. Two soil classes are foreground in terms of basin deposits, which are C and D classes. It is understood that Class C is more influenced by Gölcük trachyandesite in the southern part of the basin. The various alluvial deposits containing basin, volcanic block, gravel, sand, silt, and clay are sequenced with tuff and pomace layers. Volcanoclastic, such as tuff, tuffite, and andesite depositional system, results in higher V_{s30}. At that point, the main factor that may lead to the differentiation of ground classes is the presence of different tuff–tuffite or gravel rates in the soil content. More gravel and tuff–tuffite contents result in relatively higher seismic velocities that increase the soil class. The lithologic effect can be observed in the cross-sections A–A′ and B–B′ shown in figures 8 and 9.

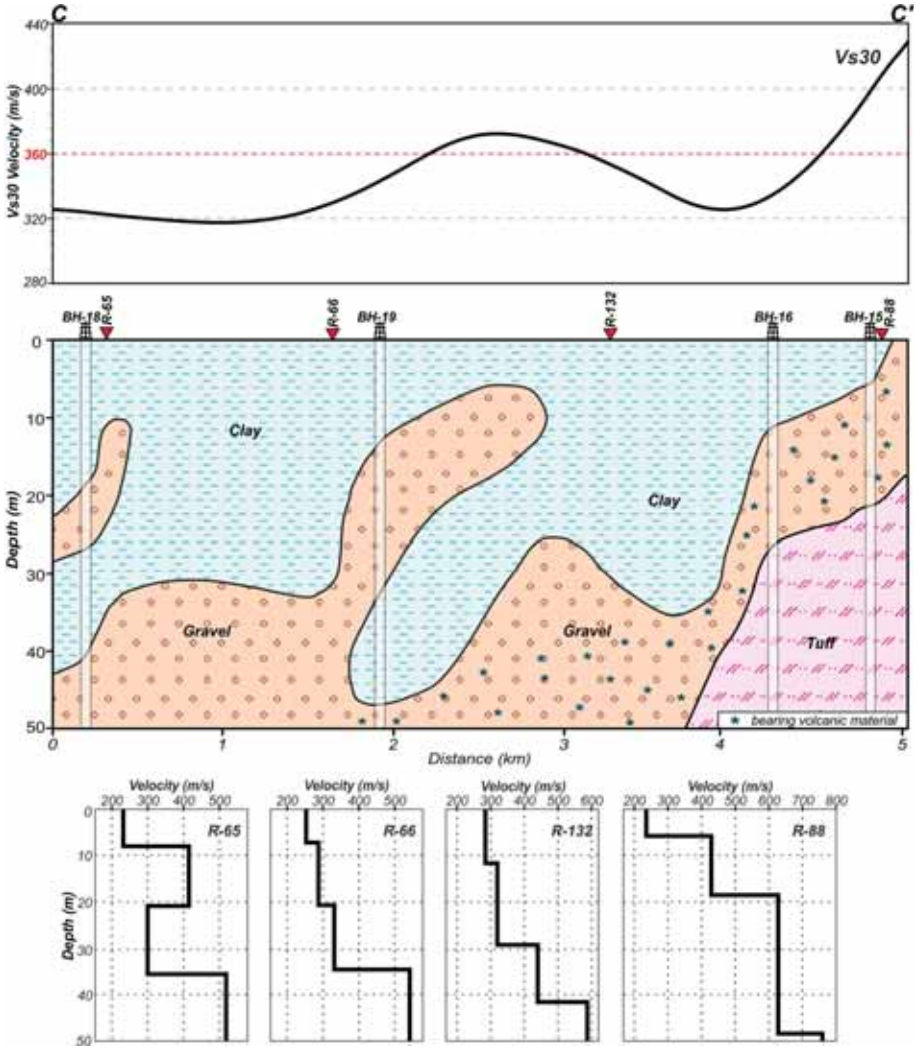

Figure 13. 2D cross-section of basin sediments the along the profile C–C′. The location is shown in figure 10. (Top panel) V_{s30} curve, (middle panel) geological cross-section, (bottom panel) 1D V_s-depth models at the borehole points.

These figures show how the shear velocity increased by the units of gravel, tuff, and andesite in the content of the soil profile. The coarse grained materials and volcanoclastic are the main factors that increases the seismic velocity and hence the soil class.

2D cross-sections were created from the obtained borehole and V_s data in 50 m depth (figures 11–13). In these figures, top, middle and bottom panels shows V_{s30}, geological units and V_s-depth profiles along the cross-sections, respectively. The lines of the cross-sections, AA', BB', CC', were selected around the locations covering mostly the borehole points (figure 10). To detect the effect of geological units on the V_s velocity, we divided them into three groups. The geologic units were grouped as sand-clay, gravel, and tuff–tuffite. The geological units sand and clay distribution, represented by light yellow and light blue colors, are observed in the D class soil distribution. The geological units gravel and tuff distribution, represented by light brown and light pink colors, are observed in the C class soil distribution (middle panel in figures 11–13). The clay unit is accumulated mostly in the eastern part of the basin. On the other hand, the sand unit is accumulated overlying the clay accumulation at the western part of the basin. Therefore, these two loose units may be the primary reason for the lowest V_{s30} value of the uppermost surface at that area. The gravel is observed everywhere in the basin. However, it can be observed that the gravel content decreases toward the surface. This unit is particularly dominated at 20 m depth below the basin. The geologic unit tuff–tuffite distribution is observed in the south and east of the basin. These areas correspond to the residential area of Isparta city in the basin. There is almost no tuff-tuffite units in soil class D determined in the soil

classification map (figure 10), and it is observed that the existence of these units in the soil content makes the soil class rise to C. There is good correlation among V_{s30}, geological units and V_s-depth profile in 50 m along the cross-sections shown in figures 11–13. This comparison represents that, while sand-clay content decreases the shear wave velocities, gravel and tuff–tuffite increases. The basin deposits generally correspond to soil classes D and C. It is observed that the gravel, tuff–tuffite content, and their proximity to the surface increase the V_{s30} and hence the soil class.

6. Conclusion

In this study, the soil classification map of Isparta basin was prepared by using V_{s30} structure and NEHRP criteria. Also, the borehole records were evaluated to compare the V_s and geological units distribution of the basin. The classification map showed that the soft alluvial deposits of the central basin are mostly classified as D, and a few areas are classified as C. The soil class at the southern part of the basin (old urbanization area of the city) increases to C class due to the increasing the tuff–tuffite content. The rock units such as Mesozoic carbonates and Cenozoic flysch located around the basin are classified as A. The soil class B is located between the class A rocks and the basin. The only difference from the class A soil is the thin alluvial slope deposit overlying the rock. The results of V_{s30} and site classification map from this study may contribute to future urban planning in the basin. However, the building design requires more detailed investigation of the area at the alluvial sediment areas where the bedrock is deeper than 30 m. The results also may contribute to the seismic risk assessment, however, need more parameters such as the bedrock depth, dominant frequency, and amplification of the site.

Acknowledgements

The authors would like to thank Scientific and Technological Research Council of Turkey (TUBITAK) for the financial support given under project no. 114Y836. In addition, the data, which were collected for this paper, will be used in Ali SİLAHTAR's PhD thesis at the Institute of Natural and Applied Sciences in Sakarya University.

References

Abrahamson N and Silva W 2008 Summary of the Abrahamson and Silva NGA ground motion relations; *Earthq. Spectra* **24/1** 67–97.

Akbulut A 1980 Eğirdir Gölü güneyinde Çandır (Sütçüler-Isparta) yöresindeki Batı Torosların jeolojisi; *Geol. Bull. Turkey* **23/1** 1–9 (in Turkish).

Aktug B, Kaypak B and Çelik R N 2010 Source parameters for the $M_w = 6.6$, 03 February 2002, Çay Earthquake (Turkey) and aftershocks from GPS, southwestern Turkey; *J. Seismol.* **14** 445–456.

Ambraseys N N and Finkel C F 1987 Seismicity of Turkey and neighbouring regions, 1899–1915; *Ann. Geophys. B-Terr. P.* **5/6** 701–726.

Ambraseys N N 1988 Engineering seismology, part I; *Earthq. Eng. Struct. Dyn.* **17** 1–50.

Anderson J G, Lee Y, Zeng Y and Day S 1996 Control of strong motion by the upper 30 meters; *B. Seismol. Soc. Am.* **86/6** 1749–1759.

Blumenthal M 1963 Le systeme structural du Taurus sud-anatolien; In: *Livre a'memoire du Professeur P. Fallot*; *Mem. Soc. Geol. Fr.* **2** 611–662.

Borcherdt R D 1970 Effects of local geology on ground motion near San Francisco Bay; *B. Seismol. Soc. Am.* **60** 29–61.

Borcherdt R D 1994 Estimation of site-dependent response spectra for design methodology and justification; *Earthq. Spectra* **10** 617–653.

Building Seismic Safety Council (BSSC) 2003 *NEHRP Recommended Provisions for seismic regulations for new buildings and other structures, Part 1: Provisions, FEMA 368*,. Federal Emergency Management Agency, Washington, DC.

Code P 2005 Eurocode 8: Design of structures for earthquake resistance–part 1: General rules, seismic actions and rules for buildings; *Brussels: European Committee for Standardization.*

Emre Ö, Duman T Y, Doğan A, Özalp S, Tokay F and Kuşçu İ 2003 Surface Faulting Associated with the Sultandağı Earthquake (M_w 6.5) of 3 February 2002, southwestern Turkey; *Seismol. Res. Lett.* **74/4** 382–392.

Görmüş M and Özkul M 1995 Gönen-Atabey (Isparta) ve Ağlasun (Burdur) Arasındaki Bölgenin Stratigrafisi; *Süleyman Demirel Univ. J. Nat. Appl. Sci.* **1** 43–64 (in Turkish).

Gutnic M and Poisson A 1970 Un Dispositif Remarkuable des Chaines Tauriques dans le Sud de la Courbure d'Isparta (Turquie meridion bale); *Comptes Rendus Academie des Sciences Paris* **270** 672–675.

Kanbur Z, Görmüş M and Kanbur S 2008 Isparta Yerleşim Alanı Kuzey Kesiminin Sığ S-Dalgası Kesitinin Çıkarılmasında Kırınım-Mikrotitreşim Tekniğinin (ReMi) Kullanılması; *Bull. Earth Sci.* **29/2** 76–86 (in Turkish).

Karaman M E, Meriç E and Tansel İ 1988 Çünür (Isparta) Dolaylarında Kretase-Tersiyer Geçişi; *Akdeniz University, J. Isparta Eng. Facul.* **4** 80–100 (in Turkish).

Koçyiğit A and Özacar A 2003 Extensional Neotectonic regime through the NE edge of the outer Isparta Angle, SW Turkey, New field and seismic data; *Turk. J. Earth Sci.* **12** 67–90.

Koçyiğit A and Deveci Ş 2007 A NS-trending active extensional structure, the Şuhut (Afyon) graben:

Commencement age of the extensional neotectonic period in the Isparta Angle, SW Turkey; *Turk. J. Earth Sci.* **16/4** 391–416.

Louie J N 2001 Faster, Better: Shear-wave velocity to 100 Meters depth from refraction microtremor arrays; *B. Seismol. Soc. Am.* **9/12** 347–364.

Louie J N, Pancha A and Pullammanappallil S 2017 Applications of Refraction Microtremor done right, and pitfalls of microtremor arrays done wrong; 16th World Conference on Earthquake Engineering (16WCEE), Santiago, Chile, Paper no. 4947, 12p.

McKenzie D P 1972 Active tectonics of the Mediterrenian region; *Geophys. J. R. Astr. Soc.* **30** 109–185.

McMechan G A and Yedlin M J 1981 Analysis of dispersive waves by wave-field transformation; *Geophysics* **46/6** 869–874.

Odum J K, Stephenson W J, Williams R A and von Hillebrandt-Andrade C 2013 V_{s30} and spectral response from collocated shallow, active-, and passive-source V_s data at 27 sites in Puerto Rico; *B. Seismol. Soc. Am.* **103/5** 2709–2728.

Optim 2006 User's manual: SeisOpt ReMi version 4.0, Optim. Inc. Reno, NV, 85.

Pancha A, Pullammanappallil S K, West L T, Louie J N and Hellmer W K 2017a Large-scale earthquake-hazard class mapping by parcel in Las Vegas Valley, Nevada; *B. Seismol. Soc. Am.* **107/2** 741–749.

Pancha A, Pullammanappallil S, Louie J N, Cashman P H and Trexler J H 2017b Determination of 3D basin shear-wave velocity structure using ambient noise in an urban environment: A case study from Reno, Nevada; *B. Seismol. Soc. Am.* **107/6** 3004–3022.

Poormirzaee R and Moghadam R H 2014 Determination of S-wave structure via refraction microtremor technique in urban area: A case study; *J. Tethys.* **2/4** 347–356.

Pullammanappallil S, Honjas W and Louie J N 2003 Determination of 1-D shear wave velocities using the refraction microtremor method; In: *Proceedings of the third international conference on the application of geophysical methodologies and NDT to transportation and infrastructure*, Orlando, Florida.

Rodriguez-Marek A, Bray J D and Abrahamson N A 2001 An empirical geotechnical seismic site response procedure; *Earthq. Spectra* **17** 65–87.

Saito M 1979 Computations of reflectivity and surface wave dispersion curves for layered media; I, Sound wave and SH wave; *Butsuri-Tanko* **32(5)** 15–26.

Saito M 1988 Compound matrix method for the calculation of spheroidal oscillation of the Earth; *Seismol. Res. Lett.* **59** 29.

Silahtar A, Budakoğlu E, Horasan G, Yıldırım E, Küyük HS, Yavuz E and Çaka D 2016 Investigation of site properties in Adapazarı, Turkey, using microtremors and surface waves; *Environ. Earth Sci.* **75/20** 1354, https://doi.org/10.1007/s12665-016-615-y.

Singh A P, Shukla A, Kumar M R and Thakkar M G 2017 Characterizing surface geology, liquefaction potential, and maximum intensity in the Kachchh seismic zone, Western India, through microtremor analysis; *B. Seismol. Soc. Am.* **107(3)** 1277–1292.

Stephenson W J, Louie J N, Pullammanappallil S, Williams R A and Odum J K 2005 Blind shear-wave velocity comparison of ReMi and MASW results with boreholes to 200 m in Santa Clara Valley: Implications for earthquake ground motion assessment; *B. Seismol. Soc. Am.* **95/6** 2016–2506.

Şengör C and Yılmaz Y 1981 Tethyan evolution of Turkey: A plate tectonic approach; *Tectonophys.* **75/(3–4)** 181–241.

Taymaz T and Price S P 1992 The 1971 May 12 Burdur Earthquake Sequence, SW Turkey: A Synthesis of Seismological and Geological Observations; *Geophys. J. Int.* **108** 589–603.

Taymaz T, Tan O and Yolsal S 2004 Seismotectonics of western Turkey: A synthesis of source parameters and rupture histories of Recent earthquakes; AGU Fall Meeting, Session T14, San Francisco-California, EOS Transactions **85/47.**

Thorson J R and Claerbout J F 1985 Velocity-stack and slant-stack stochastic inversion; *Geophysics* **50** 2727–2741.

Uniform Building Code 1997 (UBC97) International Conference of Building Officials, USA.

Utkucu M, Pınar A and Alptekin Ö 2002 A detailed slip model for the 1995, October 1, Dinar, Turkey, earthquake ($M_s = 6.1$) determined from inversion of teleseismic P and SH waveforms; *Geophys. J. Int.* **151** 184–195.

Corresponding editor: Munukutla Radhakrishna